ROYAL SOCIETY
OF CHEMISTRY

PAPER

Check for updates

Lattice vibration modes and electron–phonon interactions in monolayer *vs.* bilayer of transition metal dichalcogenides

E. Menéndez-Proupin, ⓘ *a E. Suárez Morell, ⓘ ab G. E. Marques ⓘ c and C. Trallero-Giner ⓘ c

Transition metal dichalcogenides are at the center of intense scientific activity due to their promising applications, as well as the growing interest in basic research related to their electronic and dielectric properties. The layered structure of single-(ML) and two-layer (2ML) samples presents exciting features for light–matter interaction, electron transport, and electronic and optoelectronic applications. Lattice vibrations and electron–phonon interactions are essential for studying the above mentioned topics. Phonon spectra in ML and 2ML of MoX_2 and WX_2 (X = S, Se, and Te) families are studied using first principles calculations. A comprehensive analysis of the two-dimensional optical–phonon dispersion laws is performed, and the results illustrate the main differences between ML and 2ML for each considered semiconductor. Taking advantage of *ab initio* calculations, a generalization of the phenomenological Born–Huang dielectric model for long-wavelength vibrational modes around the Γ-point of the Brillouin zone (BZ) in 2ML structures is implemented. Explicit expressions are derived for the optical phonon dispersion of in-plane and out-of-plane normal modes. The set of characteristic parameters describing each long-wavelength optical branch is resolved from a direct comparison with the exact dispersion laws provided using the first principles calculations. The long-range electron–phonon Pekar–Fröhlich (PF) interaction and intra-valley electron scattering rates at the *K*-point of the BZ *via* E′ (LO) and E_{ul} longitudinal optical oscillations are examined for the ML and 2ML structures, respectively. The non-local macroscopic screening and the coupling between the in-plane electric field and longitudinal optical mechanical oscillation, profoundly affect the PF Hamiltonian and the carrier inverse relaxation time.

I. Introduction

Transition metal dichalcogenides (TMDs) are an important class of materials in two dimensions (2D);[1] they can be represented by the formula MX_2, where M (Mo or W) is the transition metal element and X the chalcogenides (S, Se, or Te). In the X-M-X structure, the chalcogenide atomic layers are separated by a layer of metal atoms, forming a sandwich structure similar to two stacked hexagonal layers. The stacking can preferably form three polytypes: 2H hexagonal honeycomb, 1T trigonal, or 3R rhombohedral.[2,3] Unlike graphene (zero band gap), the electronic structure of TMDs possess gaps around 1–2 eV;[4] for instance, bulk MoS_2 possesses an indirect band gap of 1.3 eV, while the monolayer (ML) possesses a direct gap of 1.8 eV.[5–7]

TMDs have shown promise as a potential replacement for silicon-based electronics due to their high carrier mobility,[8] on/off ratio field-effect transistors,[9] and compatibility with existing semiconductor manufacturing processes. Due to their unique optical properties,[10] they are also being explored for use in various optoelectronic devices,[11] such as solar cells,[12] light-emitting diodes (LEDs),[13] and photodetectors.[14] They also have potential applications in sensing technologies, gas sensing[15] and bio-sensing,[16] due to their high surface-to-volume ratio and sensitivity to changes in the local environment. Furthermore, they might find applications in spintronics;[17] this field involves the manipulation of electron spin for use in information processing due to their strong spin–orbit coupling and tunable band gap.

In general, the properties of several stacked layers differ from the ML behavior.[18] For example, graphene changes from linear to parabolic dispersion,[19] and even if we rotate the layers,[20] unexpected phenomena such as superconductivity appear.[21] Two layers of polar materials lead to the appearance of spontaneous ferroelectric properties[22,23] in materials like hexagonal boron nitride[24,25] or TMDs.[26] By stacking two ferromagnetic

a Departamento de Física Aplicada I, Escuela Politécnica Superior, Universidad de Sevilla, Seville, E-41011, Spain. E-mail: emenendez@us.es

b Grupo de Simulaciones, Departamento de Física, Universidad Técnica Federico Santa María, Casilla 110-V, Valparaíso, Chile

c Departamento de Física, Universidade Federal de São Carlos, 13.565-905, São Carlos, São Paulo, Brazil

layers, we can control the magnetic phase of the system with an external electric field.[27,28] In addition to ferroelectricity applications, 2ML, and multilayer TMDs exhibit a higher density of states, carrier mobility, and stability at room temperature, giving them superior performance in various applications.[29–34]

For studies of electronic transport,[35] optoelectronic applications,[36,37] phonon damping,[38] limited phonon mobility,[39] quantum phononics,[40] magneto-polaron resonances,[41] dielectric and optical properties,[42] in 2D structures, it is necessary to address the role of the phonon spectra and its interactions with charge carriers in these novel materials. The layered single and 2ML structures present interesting features for light–matter interactions and the aforementioned topics. Optical phonons in the ML of TMD are known to play a central role in several processes.[43–45]

Furthermore, the strength of the electron–phonon interaction must depend on the environment and the number of layers of the TMD compound. This raises several questions about what the phonon spectra, their symmetry, and the electron–phonon interaction are like for a ML or a 2ML TMD, in addition to being able to establish the differences between both considered structures.

The main objective of this work is to describe the effects on the phonon branches of the ML *vs.* 2ML in TMD semiconductors. To accomplish this task, in this article we have employed density functional perturbation theory (DFPT) to obtain the complete phonon spectra of MX_2 compounds. The developed microscopic calculations support a phenomenological approach to simulate the small moment limit for optical phonon scattering laws in bilayers. We divided the study into polar and non-polar modes for the in-plane and out-of-plane atom oscillations for better analysis and comparative purposes. Having access to the analytical model within *ab initio* parameters describing the in-plane polar mode, we build the Pekar–Fröhlich (PF) Hamiltonian, allowing us to identify the key elements that govern the electron–phonon interaction.

The paper is organized as follows. First, we evaluate the phonon dispersion curves of single-layer and the bilayer of MX_2 materials based on *ab initio* calculations. We provide a detailed discussion of the symmetry properties and the main differences of the optical branches present in the ML and bilayer of the MoX_2 and WX_2 families. Employing the results obtained from first principles calculations, in Section III we generalize a phenomenological model for long-wavelength optical modes for in-plane and out-of-plane TMD bilayer oscillations. Based on the *ab initio* results of the normal optical modes, we report the characteristic parameters that support the long-wavelength model for each phonon symmetry of MoX_2 and WX_2 materials. Finally, Section IV is devoted to the evaluation of the electrons' intra-valley relaxation time due to the longitudinal phonon of ML and 2ML WX_2 compounds. We use the first principles formalism to derive the electron–phonon PF interaction Hamiltonian and compare the single-layer's scattering rates *versus* the bilayer. The conclusions are listed in Section V. Appendixes A–D report the parameters obtained by the DFPT calculations and summarize the main results for the polar modes in the framework of the phenomenological model.

II. Phonon dispersion

The phonon dispersion was computed using DFPT[46] as implemented in the Quantum Espresso package.[47] The exchange and correlation functional with dispersion interaction optB86b-vdW[48,49] was used. The projector augmented wave method was used for the electron–core interaction with standard potential files from PSLibrary version 1.0.0.[50] Periodic boundary conditions are implicit in Quantum Espresso. The supercell included a vacuum region to simulate the bidimensionality of ML and 2ML; also, a 2D cutoff was applied to the Coulomb interaction.[51] The vacuum width was initially 10 Å, but it was enlarged to ensure that the out-of-plane components of the stress tensor are also less than 1 kbar. Tables 3 and 4 report the most important parameters. The atomic positions and in-plane lattice vectors were relaxed until all force components were smaller than 0.001 Ry/bohr, and all stress tensor components were smaller than 1 kbar. The out-of-plane dimension of the simulation cells (vector c), which control the vacuum widths, were kept fixed during the relaxation. The final lattice vectors are given in Table 3.

The complete phonon dispersion laws of ML and 2ML of MoX_2 and WX_2 (X = S, Se, Te) are shown in Fig. 1–3. First, notice that for each TMD, the 2ML spectrum is quite similar to the ML one. The main differences between both structures are: (1) small band splittings, (2) the appearance of low-frequency optical bands (less than 50 cm^{-1}), (3) the branch of acoustic flexural mode – seen in quadratic dispersion around Γ – looks steeper in the bilayers, which is expected due to increased resistance to bending compared to ML. Other differences that can be appreciated in zoomed-in plots, concerning behavior at low wavevector, will be discussed below.

The symmetry groups of the Γ-point normal modes are D_{3h} and D_{3d} for the ML and 2ML, respectively.[52] For a ML there are six optical modes that for a small wavevector are divided into three classes: longitudinal in-plane modes (LO_1 and LO_2), transverse in-plane modes (TO_1 and TO_2) and out-of-plane modes (ZO_1 and ZO_2).[53] These modes correspond to the following irreducible representations of the group D_{3h}: E' (LO_2 and TO_2), E'' (LO_1 and TO_1), A'_1 (ZO_2) and A''_2 (ZO_1). The patterns of these modes are shown in Fig. 4, while labels indicate their location in the spectra of Fig. 1–3. For each branch of a ML, there are two normal modes of the 2ML. Hence, we have twelve long-wave optical branches: eight vibrating in-plane with symmetries E_g and E_u and four modes oscillating out-of-plane with symmetries A_{1g} and A_{2u}. Three low-frequency optical modes result from combining acoustical modes from the two layers. These modes are not discussed in this article. The vibration patterns displayed in Fig. 4 allow us to understand some trends in the family. In the normal modes E'' (E_u, E_g) and A'_1 (A_{2u}, A_{1g}) in the ML (2ML), the anions move, while the cation is at rest. The obtained frequencies of each mode differ in less than 4% between MoX_2 and WX_2. This can be understood if the interatomic force constants are nearly identical for Mo and W with the same anion. On the other hand, in the modes E' (E_u, E_g) and A''_2 (A_{2u}, A_{1g}), the cation motion opposes the motion of the anions. As discussed below, this motion is associated with the
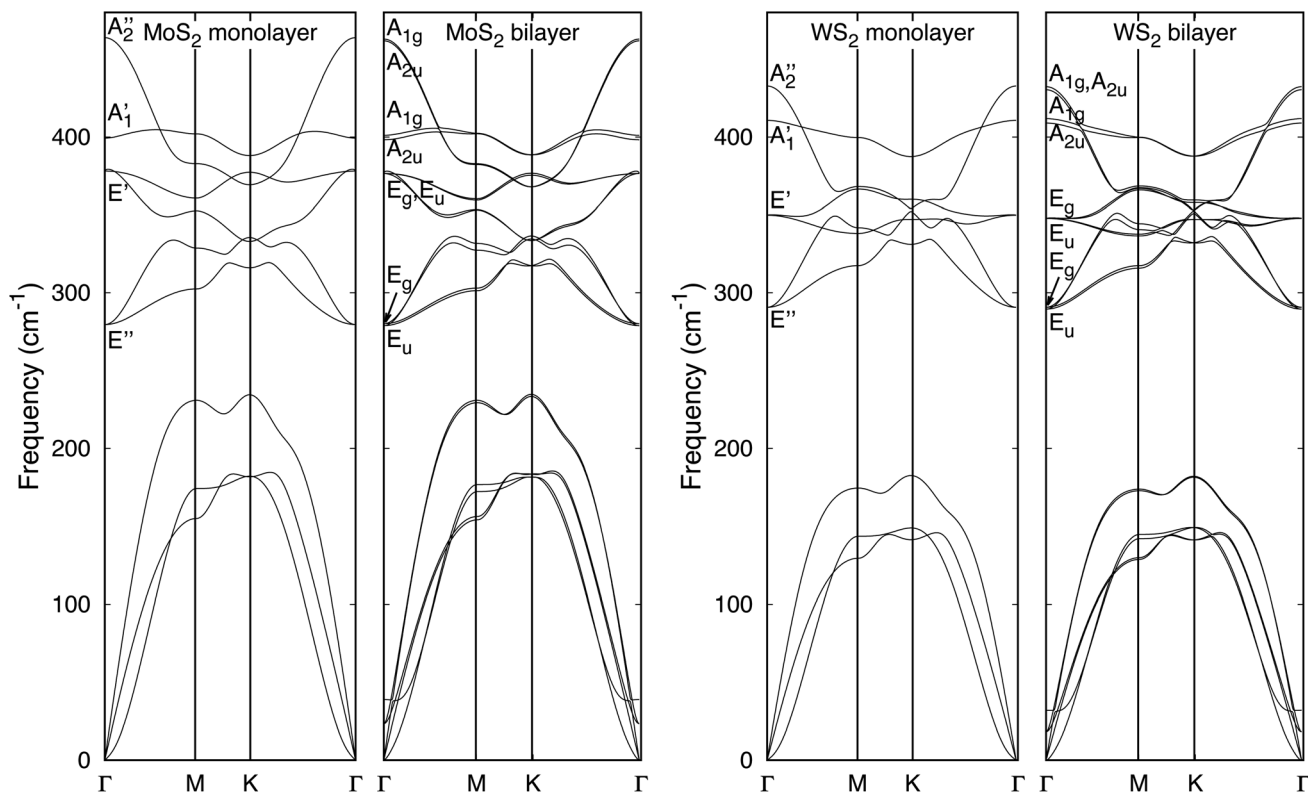
Fig. 1 Phonon dispersion curves of ML and 2ML of MoS_2 and WS_2 employing DFPT. Phonon momenta are along the high symmetry path Γ–M–K–Γ.
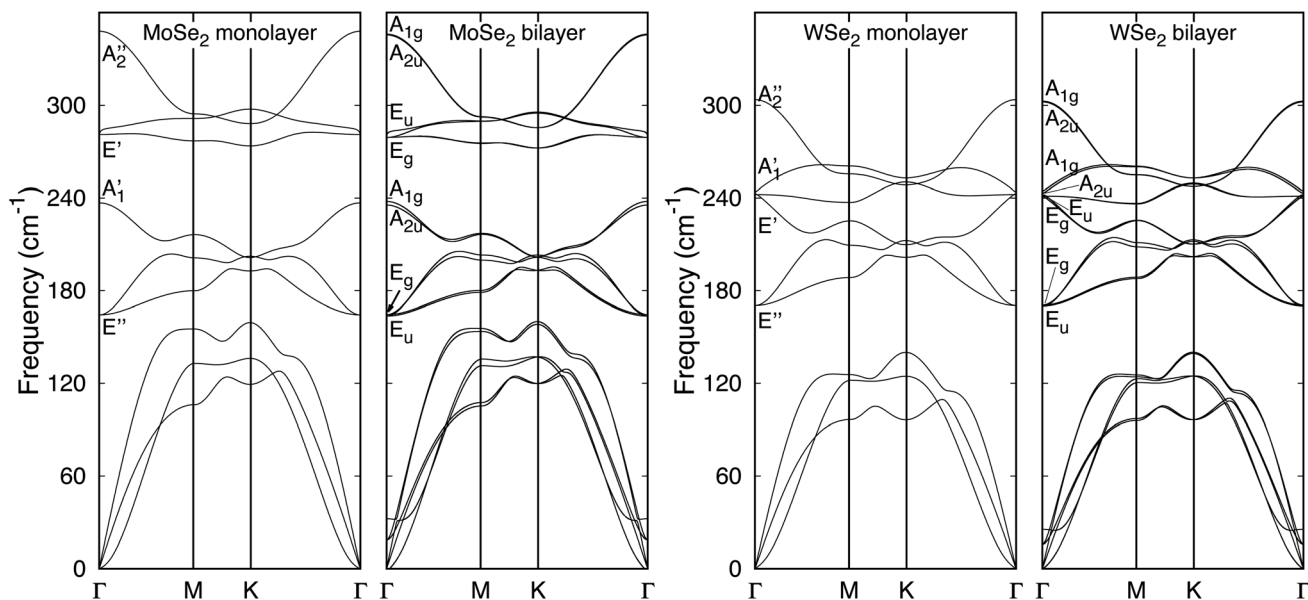

Fig. 2 DFPT phonon spectra of ML and 2ML of $MoSe_2$ and WSe_2.

reduced mass μ given by $1/\mu = 1/m_M + 1/(2m_X)$. Assuming again that the interatomic force constants do not depend on the cation, the frequency of these modes is proportional to $1/\sqrt{\mu}$. Renormalizing the frequencies of MoX_2 modes by the factor $\sqrt{\mu(MoX_2)/\mu(WX_2)}$ provides an approximation to the

frequencies of WX_2. When the anion is changed, rescaling by the reduced mass leads to increased errors, suggesting that the force constants depend more strongly on the nature of the anion than the nature of the cation. Even then, the reduced mass helps to understand another trend. The frequencies in the
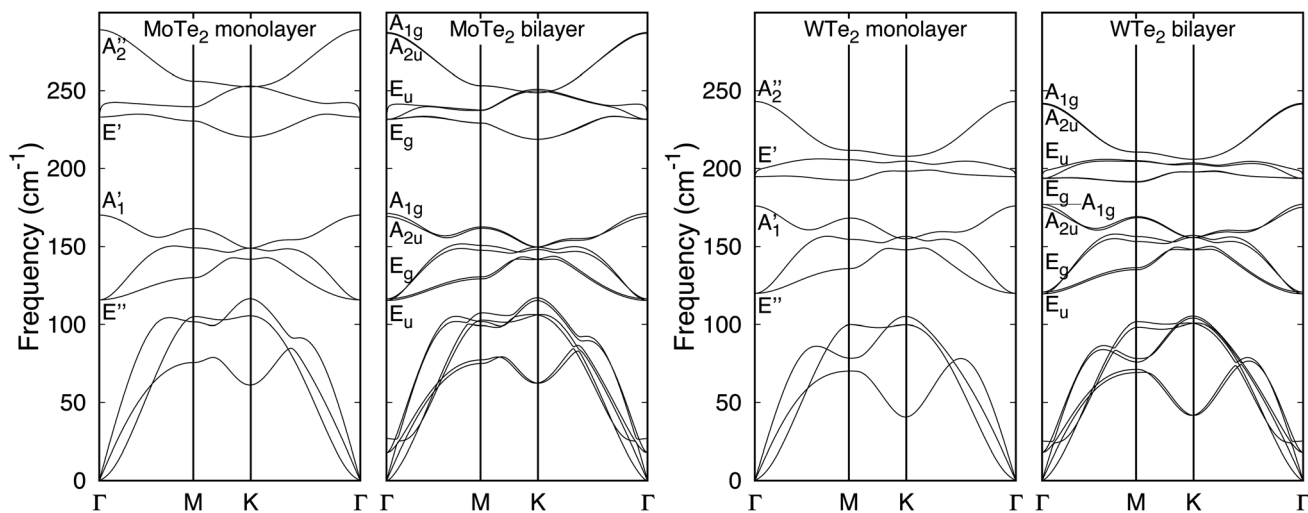
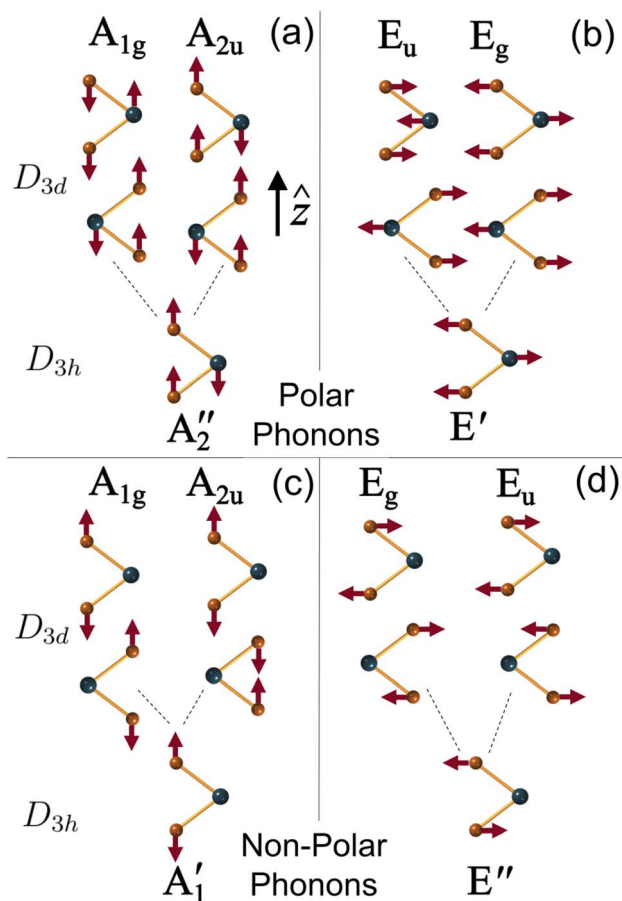Fig. 3 DFPT phonon spectra of ML and 2ML of MoTe$_2$ and WTe$_2$.

Fig. 4 Atomic displacement patterns and symmetries of phonon branches for the ML and 2ML of the MX$_2$ samples. Vibrations involving only the anion atoms (orange dots) are non-polar modes, while those cation oscillations opposing the anions' motion (dark green dots) are polar. Each mode in a bilayer has two independent modes vibrating in and out of phase. The oscillations are divided into two independent groups: polar and non-polar phonons.

sulfide monolayers increase in the order E″, E′, A′$_1$, A″$_2$. However, the order E′, A′$_1$ is reversed in MoSe$_2$ and the tellurides. For A′$_1$ frequencies, the atomic mass rescaling factor $\sqrt{m(S)/m(X)}$ is 0.64 and 0.5 for X = Se and Te, respectively. For the E′ frequencies, the reduced mass scaling factor $\sqrt{\mu(MoX_2)/\mu(WX_2)}$ is 0.80 and 0.74 for X = Se and Te, respectively. Hence, the A′$_1$ frequency decreases more than the E′ frequency due to the mass rescaling factor. Moreover, in the case of WSe$_2$, both A′$_1$ and E′ become almost degenerate (242 vs. 239 cm^{-1}).

III. Long wavelength optical modes in TMD bilayers

In ref. 53, we developed a phenomenological continuum approach, based on *ab initio* calculations, that allowed us to describe the 2D optical vibrations of several TMD monolayers. We thoroughly analyzed the long wavelength phonon dispersion curves for in-plane and out-of-plane oscillations. In this section, we generalize this model to evaluate the optical vibration modes in TMD 2MLs.

A. Basic equations

The point group D_{3d} presents an inversion center (see Fig. 4), so the phonon oscillation patterns can be classified in-phase and anti-phase. Next, the oscillation vectors U_{ip} and U_{ap} will describe the in-phase and anti-phase motion of the atoms for the two independent normal modes. The 2D TMD unit cell is unfolded into two single sub-cells I and II with a van der Waals interaction. Therefore, we can construct the normal oscillations for the bilayer by combining the in-phase or anti-phase motion of the individual sub-cells I and II. These two combinations have different symmetry representations with similar optical phonon dispersion, and due to the weak interlayer van der Waals coupling, they must show almost the same phonon energies.

B. Modes vibrating out-of-plane

Out-of-plane vibrations have A-symmetry. For the sake of clarity, we divide the study into two groups: (i) polar and (ii) non-polar modes (see normal vibration patterns in Fig. 4(a) and (c)).

1. A_{1g} and A_{2u}-non-polar phonons. Following the oscillation pattern shown in Fig. 4(c), the mass of the metal atoms M_i ($i = 1$, 2) are at rest, while only the chalcogen atoms (x_1, x_2) and (x_3, x_4) located at the first and second layer vibrate. The relative vector displacements $U_I = (u_{x_1} - u_{x_2})/2$ and $U_{II} = (u_{x_3} - u_{x_4})/2$ describe the opposing motion of the two chalcogen atoms X_i ($i = 1$, 2 or 3, 4) in the single-layer of reduced mass $\mu^{-1} = 2/m_X$. The anti-phase and in-phase displacements are given by $U_{ap} = (U_I - U_{II}/2$ and $U_{ip} = (U_I + U_{II})/2$. The mechanical equation of motion reads as

$$\rho_m \omega^2 U = \gamma \cdot U \pm \beta [\nabla \nabla \cdot U - \nabla \times \nabla \times U], \quad (1)$$

where

$$\gamma = \rho_m \begin{pmatrix} \omega_{A_{1g}} & 0 \\ 0 & \omega_{A_{2u}} \end{pmatrix}; \beta = \rho_m \begin{pmatrix} \beta^2_{A_{1g}} & 0 \\ 0 & \beta^2_{A_{2u}} \end{pmatrix}; U = \begin{pmatrix} U_{ip} \\ U_{ap} \end{pmatrix},$$

$\omega_{A_{1g}}$ and $\omega_{A_{2u}}$ are the natural frequencies at phonon wave vector $q = 0$ with symmetry A_{1g} and A_{2u}, respectively, ρ_m is the 2D reduced mass density of a single-layer, β a tensor describing the quadratic parabolic behavior of phonon dispersion with q vector.

Since the vector $U(\rho)$ is parallel to the z-axis, eqn (1) decouples into two independent equations

$$\left(\omega^2 - \omega^2_{A_{1g}(A_{2u})} \right) U_{ip(ap)} = \mp \beta^2_{A_{1g}(A_{2u})} \nabla \times \nabla \times U_{ip(ap)}. \quad (2)$$

The choice of the sign $+$ or $-$ depends on the curvature of the dispersion relation of the TMD material under consideration. From eqn (2) we get the dispersion relation:

$$\omega^2 = \omega^2_{A_{1g}(A_{2u})} \pm \beta^2_{A_{1g}(A_{2u})} q^2. \quad (3)$$

2. A_{1g} and A_{2u}-polar phonons. The opposite motion of the chalcogen atoms (x_1, x_2) and (x_3, x_4) with respect to the transition metals (M_1, M_2) are responsible for the branches A_{1g} and A_{2u} (see Fig. 4(a)). The vector displacements, which describe the out-of-plane oscillation in the single layers I and II, are $U_I = u_{M_1} - (u_{x_1} + u_{x_3})/2$ and $U_{II} = u_{M_2} - (u_{x_3} + u_{x_4})/2$ with reduced mass $\mu^{-1} =$
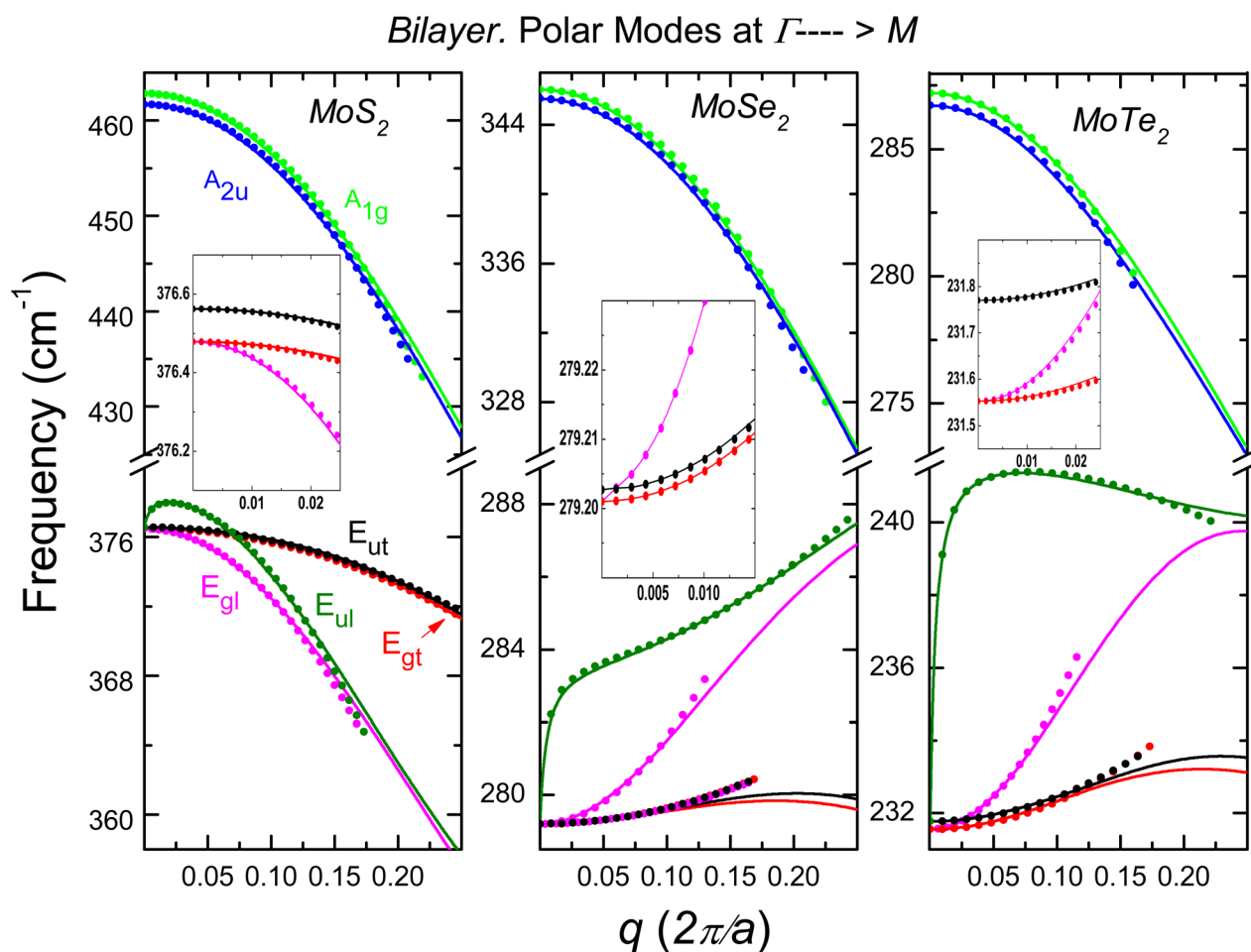

Fig. 5 Dispersion law of optical phonons for a bilayer of MoS$_2$, MoSe$_2$ and MoTe$_2$. Out-of-plane phonons: A_{1g} (green line) and A_{2u} (blue line). In-plane modes with symmetries E_g and E_u split into E_{gl} (magenta line), E_{gt} (red line), E_{ul} (olive line) and E_{ut} (black line). The insets show the phonon dispersion for the E_{gl}, E_{gt} and E_{ut} modes in the range $q \to 0$.

$m_M{}^{-1} + (2m_x)^{-1}$. The normal oscillations for the U_{ip} in-phase and the U_{ap} anti-phase correspond to A$_{2u}$ and A$_{1g}$ polar phonon modes, respectively. The relative displacement of atoms in the single-cell, I or II, or equivalently the atomic displacements U_I and U_{II}, generate a macroscopic electric field. For the in-phase oscillation U_{ip}, we are in the presence of a non-zero internal electric field E_z. This field is coupled with the mechanical displacement U_{ip}. Let us symbolize this linkage between the mechanical and the electric fields by the unknown constant $\alpha_{A_{2u}}$. The mechanical equation of motion for U_{ip} can be cast as

$$\rho_m \omega^2 U_{ip} = \rho_m \omega_{0A_{2u}}^2 U_{ip} - \alpha_{A_{2u}} E_z(\boldsymbol{\rho}, z)$$
$$\pm \rho_m \beta_{A_{2u}}^2 [\nabla\nabla \cdot U_{ip} - \nabla \times \nabla \times U_{ip}], \quad (4)$$

where $E_z(\boldsymbol{\rho},z)$ is the z-component of the electric field in the bilayer (we will assume that $E_z(\boldsymbol{\rho},z) \approx E_z(\boldsymbol{\rho},0)$), $\omega_{0A_{2u}}$ the natural frequency at $q = 0$ with symmetry A$_{2u}$, $\beta_{A_{2u}}$ represents the quadratic behavior in q of the phonon dispersion. Due to the appearance of an internal electric field to the equation of motion (4) we must add the Maxwell's equations that couples the mechanical motion U_{ip}, E_z and the z-component of the macroscopic polarization (see Appendix B). It is possible to

show that the dispersion relations for the polar phonon A$_{2u}$ vibrating out-of-plane are

$$\omega^2 = \omega_{A_{2u}}^2 \pm q^2 \beta_{A_{2u}}^2, \quad (5)$$

where $\omega_{A_{2u}}$ is the renormalized frequency at Γ. The out-of-phase amplitude U_{ap} does not produce an electric field; therefore, the total internal electric field in the bilayer can be set to zero. Consequently, we can assume a similar eqn (4) but with $E_z = 0$. Thus, for the A$_{1g}$ mode:

$$\omega^2 = \omega_{A_{1g}}^2 \pm q^2 \beta_{A_{1g}}^2, \quad (6)$$

where $\omega_{A_{1g}}$ and $\beta_{A_{1g}}$ are the natural frequency at Γ and the parabolicity parameter, respectively. Note that the A$_{1g}$ mode is Raman-allowed in the backscattering configuration with parallel configuration (X,X), and it is absent for cross-polarization (X,Y) under normal incidence.[54] In the case of a single-layer, this mode is infrared Raman (IR) active. Due to the inversion center in the bilayer, the construction of the anti-phase solution U_{ap} leads to the generation of Raman active mode A$_{1g}$.[55] This fact has been observed in WSe$_2$, TaSe$_2$, and MoTe$_2$.[56] The A$_{2u}$ phonon of the bilayer, as in the bulk, is still IR active.
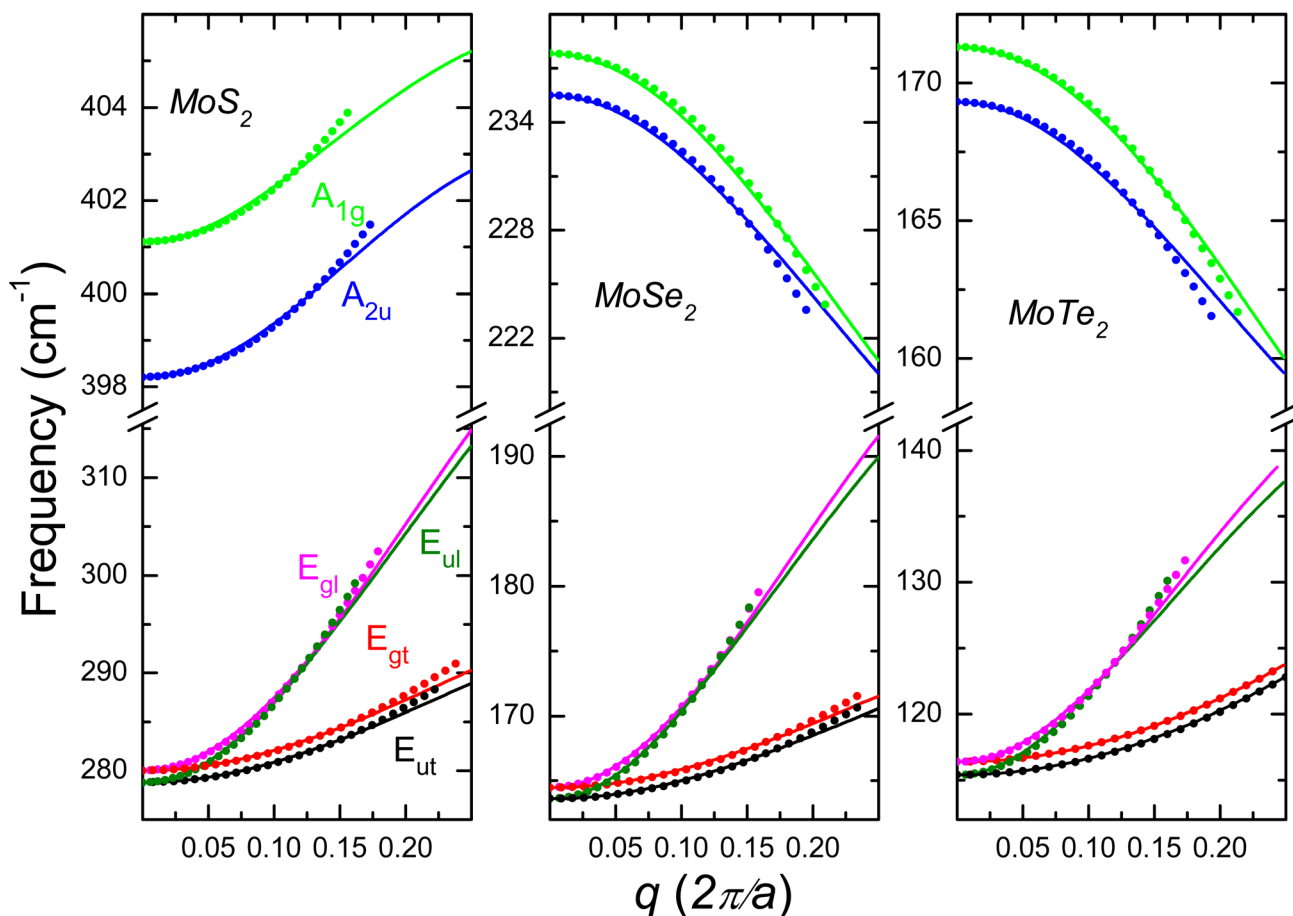

Fig. 6 The same as Fig. 5 but for the dispersion law of non-polar optical phonon dispersion.

C. Modes vibrating in-plane

In-plane phonons have E-symmetry. For the ML, the single-unit cell has two irreducible representations E′ and E″. The modes with E′-symmetry are polar, while those with E″ are non-polar (see in Fig. 4(b) and (d) the scheme of the vibration patterns and symmetries for the ML and bilayer). In general, modes vibrating in-plane have similar characteristics to those oscillating out-of-plane. Each single-layer mode has two branches of the 2ML: in-phase and anti-phase. These combinations belong to two different symmetry representations E_g and E_u. All E-modes are doubly degenerate at Γ.

1. E_u and E_g-non-polar phonons. Phonon modes with symmetry E_u and E_g are responsible for four optical branches. Two of them move in-phase and two in anti-phase of the atoms X_i ($i = 1, 2, 3, 4$) (we follow the same notation as in Subsection (III B 1)). Here, we are in the presence of two different sub-spaces that provide two independent equations of motion. A general equation of motion for the atom's in-phase and out-of-phase motion can be written as

$$\rho_m \omega^2 U = \gamma \cdot U \pm (\beta_L \cdot \nabla \nabla \cdot U - \beta_T \cdot \nabla \times \nabla \times U), \quad (7)$$

where γ, β_L (β_T) are given by

$$\gamma = \rho_m \begin{pmatrix} \omega_{E_g}^2 & 0 \\ 0 & \omega_{E_u}^2 \end{pmatrix}; \beta_L(\beta_T) = \rho_m \begin{pmatrix} \beta_{E_{gl(gt)}}^2 & 0 \\ 0 & \beta_{E_{ul(t)}}^2 \end{pmatrix},$$

ω_{E_g}, ω_{E_u} are the natural frequencies in-plane at Γ, $\beta_{E_{gl(t)}}^2$ and $\beta_{E_{ul(t)}}^2$ are the phenomenological parameters obtained by the phonon dispersion $\omega(q)$. Using the solution $U_{ip}(U_{ap}) = U_{oi}(U_{oa})e^{iq \cdot \rho}$ we get

$$\left(\omega^2 - \omega_{E_g}^2\right)U_{oi} = \pm\beta_{E_{gl}}^2 q(q \cdot U_{oi}) \pm \beta_{E_{gt}}^2 \left[-q(q \cdot U_{oi}) + q^2 U_{oi}\right]. \quad (8)$$

The same equation follows for the anti-phase component U_{oa} with $\omega_{E_g} \to \omega_{E_u}$. Taking $U_o = U_l + U_t$, where $q \cdot U_t = 0$, $q \cdot U_l \neq 0$, $q \times U_t \neq 0$, $q \times U_l = 0$ we have two branches for phonons with E_g-symmetry, longitudinal and transverse with

$$\omega_{E_{gl(gt)}}^2 = \omega_{E_g}^2 \pm \beta_{E_{gl(gt)}}^2 q^2. \quad (9)$$

For the E_u-symmetry we have the dispersion relation:

$$\omega_{E_{ul(ut)}}^2 = \omega_{E_u}^2 \pm \beta_{E_{ul(ut)}}^2 q^2. \quad (10)$$
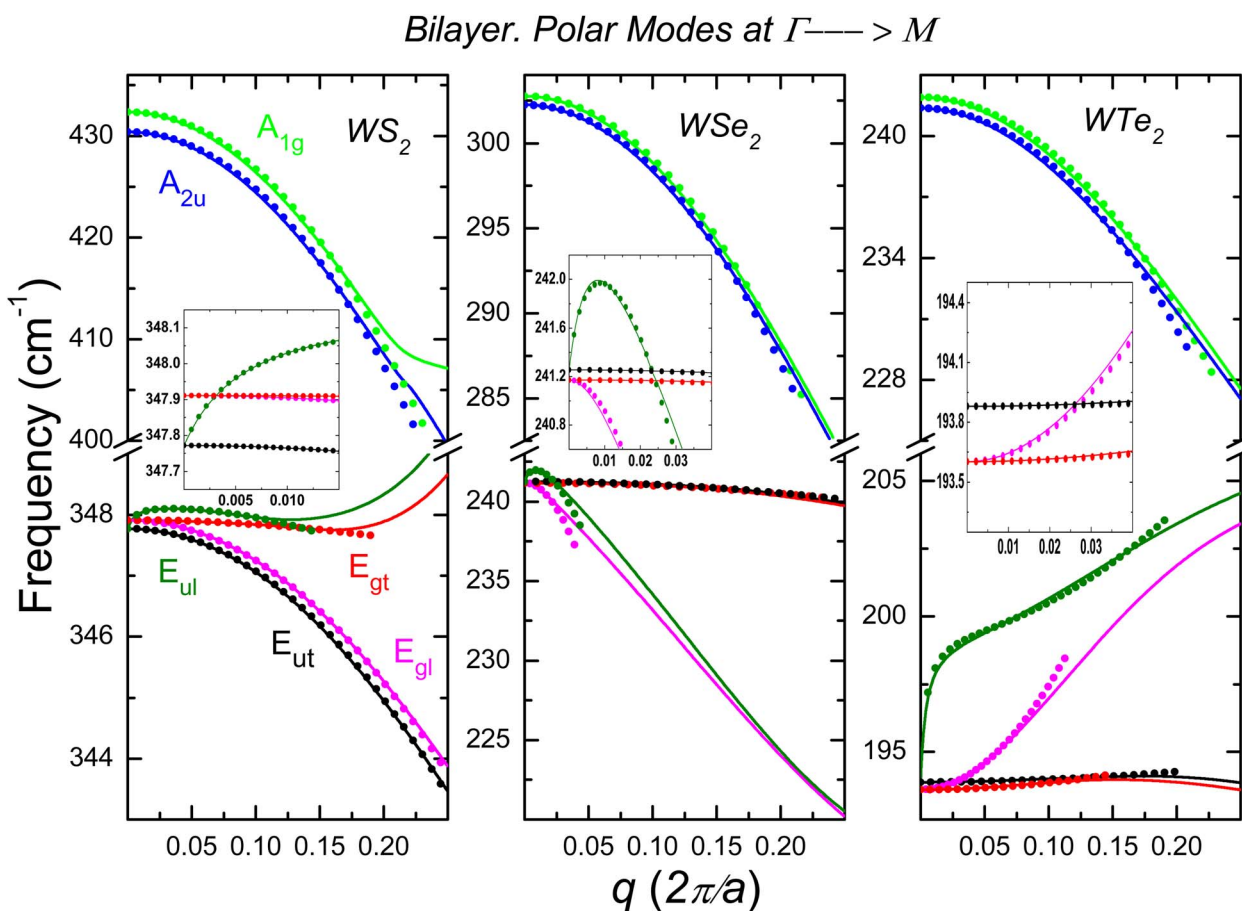
Fig. 7 Polar optical phonon dispersion for a bilayer of WS$_2$, WSe$_2$ and WTe$_2$. Out-of-plane phonons: A$_{1g}$ (green line) and A$_{2u}$ (blue line). In-plane-modes with symmetries E$_g$ and E$_u$ split into E$_{gl}$ (magenta line), E$_{gt}$ (red line), E$_{ul}$ (olive line) and E$_{ut}$ (black line). The insets show the phonon dispersion of WS$_2$ and WSe$_2$ in the range $q \to 0$, while for WTe$_2$ only the E$_{gl}$, E$_{gt}$ and E$_{ut}$ modes are shown.

2. E_u and E_g-polar phonons. Each vibration mode in a single layer of MX_2 is split into two modes in the bilayer: $E' \rightarrow 2E_g$ and $2E_u$. The movement of the in-plane phonon is determined by the oscillation of the positive ion relative to the negative ions: $U_I = u_{M_1} - (u_{x_1} + u_{x_2})/2$ and $U_{II} = u_{M_2} - (u_{x_3} + u_{x_4})/2$ for subcells I and II, that is, the M-atom vibrates opposed to the phase of the X-atoms in the layer.

E_g-phonon. Assuming that the out-of-phase amplitude U_{ap} carries no net electric field, the E_g-optical vibrations are ruled by

$$\left(\omega^2 - \omega_{E_g}^2\right)U_{ap} = \pm\rho_m\left(\beta_{E_{gl}}^2 \nabla\nabla\cdot U_{ap} - \beta_{E_{gt}}^2 \nabla\times\nabla\times U_{ap}\right), \quad (11)$$

thus, we obtain the phonon dispersion for the longitudinal and transverse phonon:

$$\omega_{E_{gl(gt)}}^2 = \omega_{E_g}^2 \pm \beta_{E_{gl(gt)}}^2 q^2. \quad (12)$$

E_u-phonon. The opposite motions of the ions M_i ($i = 1, 2$) and X_i ($i = 1, 2, 3, 4$) lead to the appearance of a 2D electric field $E(\rho, 0)$ in the plane of the two layers. The equation of motion for the in-phase vector displacement U_{ip} of the atoms involved is written as

$$\rho_m\left(\omega^2 - \omega_{E_u}^2\right)U_{ip} = -\alpha E(\rho, 0)U_{ip}$$
$$\pm\rho_m\left(\beta_{E_{ul}}^2 \nabla\nabla\cdot U_{ip} - \beta_{E_{ut}}^2 \nabla\times\nabla\times U_{ip}\right), \quad (13)$$

where α is the coupling constant between the mechanical oscillation U_{ip} and the in-plane electric field E,[53] ρ_m is the 2D reduced mass density with $\mu^{-1} = m_M^{-1} + (2m_X)^{-1}$, and ω_{E_u} the natural frequency at Γ. Eqn (13) provides the phonon dispersion relations (see Appendix C)

$$\omega_{E_{ul}}^2 = \omega_{E_u}^2 + \frac{2\pi\alpha^2}{\rho_m}\frac{q}{(1 + r_0 q)} \pm \beta_{E_{ul}}^2 q^2, \quad (14)$$

and

$$\omega_{E_{ut}}^2 = \omega_{E_u}^2 \pm \beta_{E_{ut}}^2 q^2, \quad (15)$$

with $r_0 = 2\pi\alpha_2$ being the screening parameter of the bilayer.

D. Phonon parameters

Fig. 5–8 compare *ab initio* calculations and the long-wave optical model for the MoX_2 and WX_2 families. For each family, the results are divided into polar and non-polar branches.
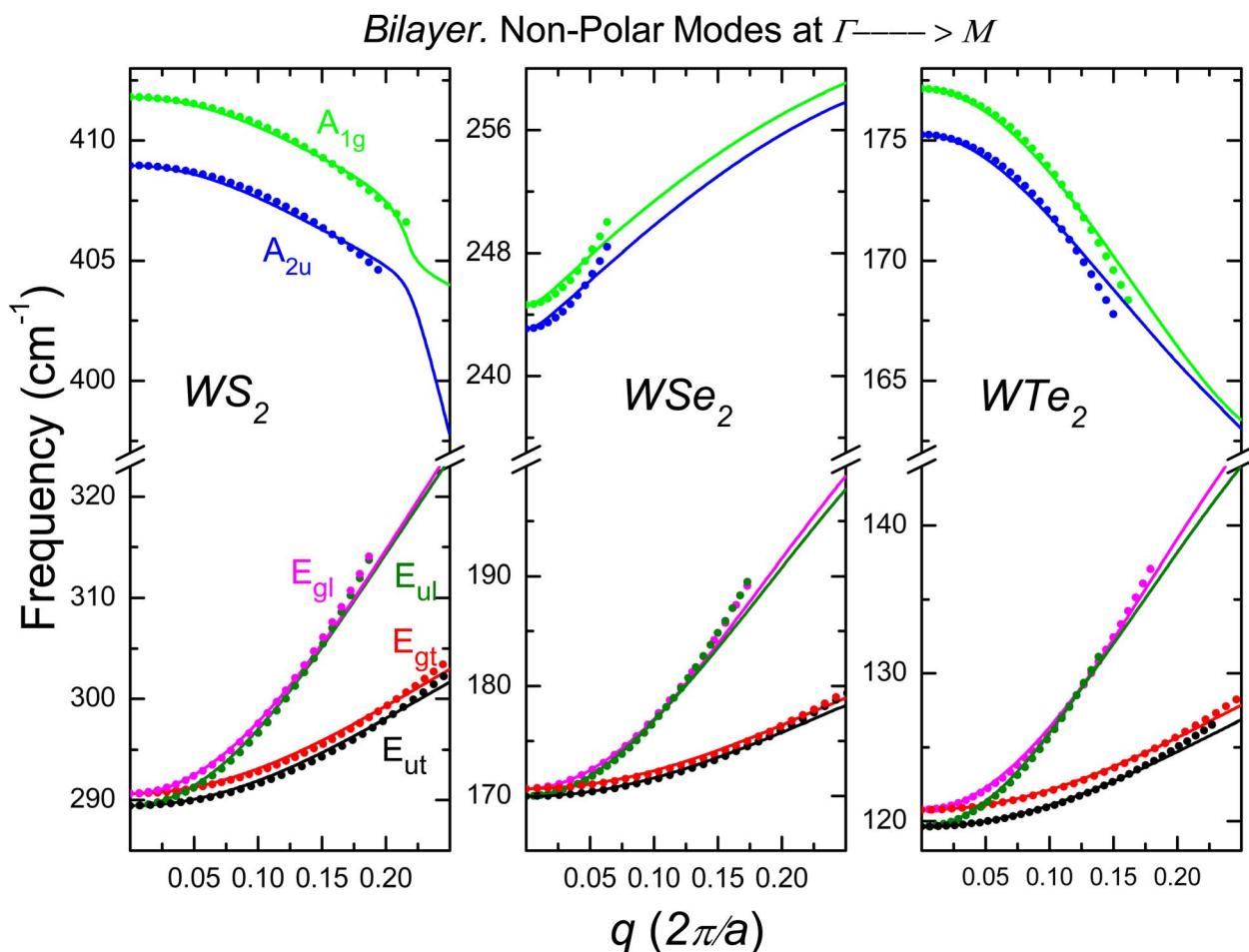

Fig. 8 The same as Fig. 7 but for the dispersion law of non-polar optical phonon dispersion.

1. MoX$_2$ family. In Fig. 5 and 6 we show the optical phonon dispersion law, $\omega(q)$ of the 2ML MoX$_2$ and phonon wave vectors $q \leq 0.25\,(2\pi/a)$. The twelve phonon modes 2A$_{2u}$, 2A$_{1g}$, 2E$_{ul}$, 2E$_{ut}$, 2E$_{gl}$ and 2E$_{gt}$ are shown along the $\Gamma \rightarrow M$-direction of the BZ. The dispersion relations obtained in Section II using the *ab initio* procedure are displayed by straight lines. The dots show the results using the long-wave polar optical model of Section III.

2. WX$_2$ family. Fig. 7 and 8 are devoted to the 2A$_{2u}$, 2A$_{1g}$, 2E$_{ul}$, 2E$_{ut}$, 2E$_{gl}$ and 2E$_{gt}$ phonon dispersion branches for 2ML of WX$_2$. We employed the same notation as Fig. 5 and 6.

The Fig. 5–8 show that the precision achieved between the phenomenological treatment and first principles calculations depends on the optical branch and the material. The in-plane branches with E$'$ (polar modes) and E$''$ (non-polar modes) symmetry are double-degenerates vibrating along the perpendicular longitudinal (E$_{gl}$, E$_{ul}$) and transverse (E$_{gt}$, E$_{ut}$) directions. Taking into account the phonon dispersion laws in Fig. 1–3, one can extract the parameters that govern the long-wave phenomenological model shown in Fig. 5–8. In Table 1, we report the relevant parameters of the twelve optical phonon branches of the 2ML.

A closer look at the results reveals that the parameters for the modes with symmetries A$_{1g}$ and A$_{2u}$ are very similar. We can argue the same for non-polar modes with E$_g$ and E$_u$ irreducible representation. For the polar phonon with E-symmetry, the situation is not uniform. The E$_{ut}$ and E$_{gt}$ dispersion laws are

Table 1 Phonon data of the 2ML MoX$_2$ and WX$_2$ (X = S, Se, and Te). The dimensionless curvatures $\mathbb{C}_\delta = \pm (2\pi\beta_\delta)^2/(a\omega_\delta(0))^2$ and $\Xi = (2\pi\alpha)^2/(a\rho_m\omega_{E_u}^2)$ are estimated from the dispersion curves and the phonon dispersion law obtained using *ab initio* calculations for polar and non-polar optical modes. ω_δ in cm^{-1}

	MoS$_2$	MoSe$_2$	MoTe$_2$	WS$_2$	WSe$_2$	WTe$_2$
Polar						
$\omega_{A_{1g}}$	462.8	346.0	287.2	432.4	302.8	241.9
$\mathbb{C}_{A_{1g}}$	−2.58	−2.0	−1.90	−2.58	−2.4	−2.1
$\omega_{A_{2u}}$	461.7	345.5	286.7	430.4	302.3	241.4
$\mathbb{C}_{A_{2u}}$	−2.6	−2.05	−1.90	−2.6	−2.45	−2.2
ω_{E_u}	376.6	279.2	231.8	347.8	241.3	193.9
$\mathbb{C}_{E_{ul}}$	−2.4	0.47	−0.35	−0.12	−17.7	1.2
Ξ	2.0	6.95	22.6	0.4	2.2	14
$\mathbb{C}_{E_{ut}}$	−0.41	0.3	0.58	−0.4	−0.15	0.1
ω_{E_g}	376.5	279.2	231.6	347.9	241.2	193.6
$\mathbb{C}_{E_{gt}}$	−0.43	0.31	0.66	−0.04	−0.14	0.26
$\mathbb{C}_{E_{gl}}$	−2.1	1.7	3.1	−0.38	−21	4.0
Non-polar						
$\omega_{A_{1g}}$	401.1	237.8	171.3	411.8	244.6	177.1
$\mathbb{C}_{A_{1g}}$	0.57	−2.6	−2.4	−0.54	11	−3.7
$\omega_{A_{2u}}$	398.2	235.5	169.3	409.0	243.1	175.2
$\mathbb{C}_{A_{2u}}$	0.55	−2.7	−2.4	−0.56	11	−3.7
ω_{E_g}	280.0	164.5	116.4	290.6	170.7	120.8
$\mathbb{C}_{E_{gl}}$	5.2	7.6	9.3	4.8	7.6	9.0
$\mathbb{C}_{E_{gt}}$	1.4	1.55	2.1	1.5	1.7	2.1
ω_{E_u}	278.8	163.6	115.4	289.4	170.0	119.6
$\mathbb{C}_{E_{ul}}$	5.8	8.2	10.6	5.0	8.1	10.5
$\mathbb{C}_{E_{ut}}$	1.4	1.6	2.12	1.5	1.8	2.3

Table 2 Phonon data of the ML MoX$_2$ and WX$_2$ (X = S, Se, and Te) obtained using *ab initio* calculations. The notation is the same as in Table 1

	MoS$_2$	MoSe$_2$	MoTe$_2$	WS$_2$	WSe$_2$	WTe$_2$
Polar						
ω_{ZO_1}	463.7	347.9	289.0	432.4	303.7	243.1
$\mathbb{C}_{ZO_1}$	−2.38	−1.9	−1.82	−2.4	−2.2	−2.05
$\omega_{E'}$	378.1	281.0	233.0	349.4	242.2	194.8
$\mathbb{C}_{LO_2}$	−2.9	0.34	−0.3	−0.19	−37	1.0
Ξ	1.06	3.5	11.5	0.23	1.3	7.2
$\mathbb{C}_{TO_2}$	−0.46	0.15	0.52	−0.42	−0.18	0.13
Non-polar						
ω_{ZO_2}	399.3	236.9	170.3	410.7	243.8	176.1
$\mathbb{C}_{ZO_2}$	0.72	−2.5	−2.25	−0.48	21	−3.2
$\omega_{E''}$	279.5	164.4	115.8	290.7	170.3	120.0
$\mathbb{C}_{LO_1}$	4.7	7.45	9.84	4.5	7.2	9.8
$\mathbb{C}_{TO_1}$	1.37	1.54	1.95	1.6	1.84	2.17

almost identical. Differences are observed for the curvatures $\mathbb{C}_{E_{ul}}$ and $\mathbb{C}_{E_{ut}}$ between the two branches, even the sign is not always preserved. These differences are determined mainly by the dielectric properties of the environment. The in-phase displacement $\boldsymbol{U}_{ip}$ creates an in-plane internal electric field that is greatly affected by the dielectric environment (see eqn (14).)

For comparison, the phonon parameters for the six branches of the single-layer are also reported in Table 2. Here, we employ the corresponding dispersion law provided by the phenomenological model[53] for the A$''_2$ (ZO$_1$), A$'_1$ (ZO$_2$), E$'$ (LO$_2$, TO$_2$), and E$''$ (LO$_1$, TO$_1$) phonon symmetries.

From the compiled values in Tables 1 and 2, we conclude the following: (1) the phonon frequencies for the polar branches in the 2ML are lower than those of the ML, while the opposite is achieved in the non-polar modes, (2) the linear dispersion relation given by the slope Ξ is double that of the ML, (3) the curvatures $\mathbb{C}_\delta$ take similar values except for the polar modes of E$_g$-symmetry. Comparing the phonon dispersion reported in ref. 53 with the data given in Table 2, we observe that the phonon parameters in both cases are almost the same. Due to incorrect manipulation, the results collected in Table 2 of ref. 53 for WTe$_2$ need to be corrected; also, the correct value for MoS$_2$ $\mathbb{C}_{TO_2} = -0.46$.

IV. Intra-valley scattering rate

The conductivity and mobility in semiconductors depends directly on the carrier's scattering rate (SR), τ^{-1}.[57] At high temperatures ($T \sim 300$ K) and carrier energies greater than those of an optical phonon, the longitudinal optical branch determines the faster relaxation time. Evaluation of the scattering rate due to the intra-valley transition in ML and 2ML of TMDs is of profound interest for transport and optoelectronic applications.[58] In this framework, we must know the dependence of the inverse relaxation time on the carrier energy E and the phonon parameters. Fermi's golden rule gives the scattering rate of the electronic transitions,
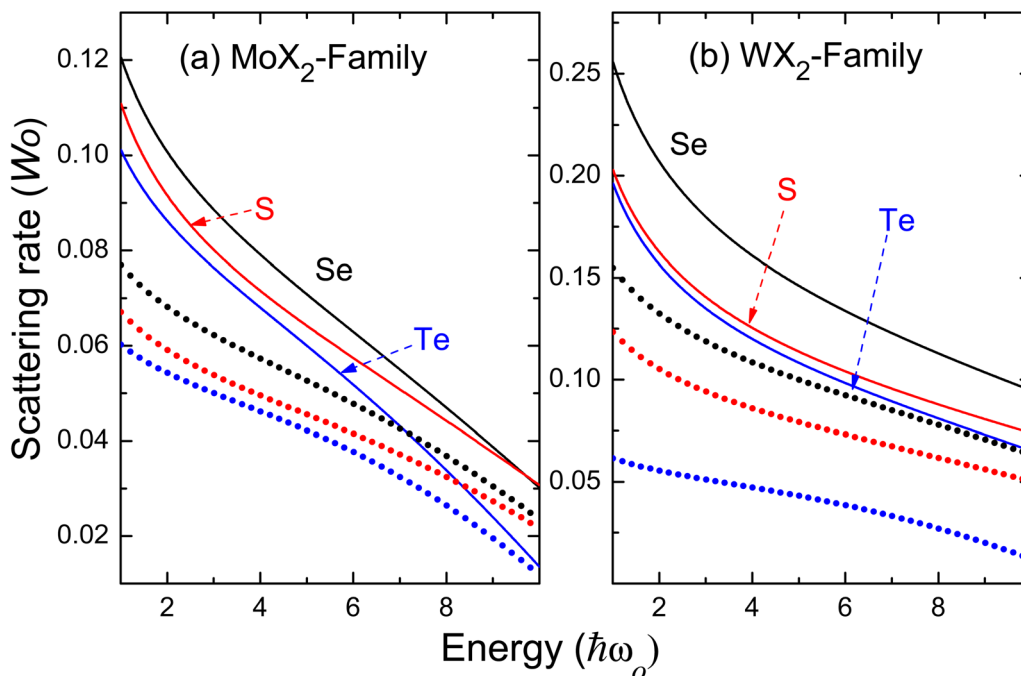
Fig. 9 Scattering rate as a function of the reduced energy $E/\hbar\omega_o$ for the (a) MoX_2 and (b) WX_2 families. Straight lines represent the ML samples ($\omega_o = \omega_{E'}$), dots correspond to 2ML materials ($\omega_o = \omega_{Eul}$). The parameters in Tables 1–3 are used, the results are given in units of W_o (20) for the ML parameters.

$$\frac{1}{\tau(\boldsymbol{k})} = \frac{2\pi}{\hbar} \sum_{q,k'} |\langle F|\hat{H}_F|I\rangle|^2 \delta(E_F - E_I). \quad (16)$$

In the initial (final) state $|I\rangle$ ($|F\rangle$) we have a particle with momentum k (k') and energy $E_I = E = \hbar^2 k^2/(2m)$ $(E_F = \hbar^2 k'^2/(2m) \pm \hbar\omega_o)$ with m being the effective mass. We consider the interaction of carriers with polarized longitudinal optical phonons $\omega_{E'}$ and ω_{Eul} for the ML and 2ML, respectively. For an evaluation of $\tau(E)$ it is necessary to derive the PF interaction Hamiltonian ($\hat{H}_{PF}$). Ref. 53 reports $\hat{H}_{PF}$ for a ML TMD and in Appendix D the corresponding electron–phonon interaction for 2ML is obtained. It is shown that the $\hat{H}_{PF}$ can be written as

$$\hat{H}_{PF} = -i \sum_q \frac{\mathbb{G}_{Ph}}{\sqrt{N_c(1+r_0 q)}} \left[\hat{b}_q e^{iq\cdot\rho} + \hat{b}_q^\dagger e^{-iq\cdot\rho}\right], \quad (17)$$

where

$$\mathbb{G}_{Ph} = \left(\frac{2\pi^2 e^2 \hbar \alpha^2}{A\rho_m\omega_o}\right)^{1/2}. \quad (18)$$

Eqn (17) is valid for both considered structures, the main difference is in the parameter values α, ω_o ($\omega_{E'}$, ω_{Eul}) and r_0. Assuming non-degenerate semiconductor and that $\omega_o(\boldsymbol{q}) = \omega_o(0)$ we get the scattering rate

$$\frac{1}{\tau(E)} = W_o[(N_o + 1)\mathcal{F}_1(E)H(E - \hbar\omega_o) + N_o\mathcal{F}_2(E)], \quad (19)$$

where N_o is the Bose–Einstein distribution function, $H(z)$ the Heaviside step function,

$$W_o = \frac{2\pi^2 e^2 \alpha^2}{\rho_m\omega_{E_o}} \frac{2m}{\hbar^2}, \quad (20)$$

$$\mathcal{F}_{1,2} = \int_{x_1^{(\mp)}}^{x_2^{(\mp)}} \frac{x}{1 + \sqrt{\frac{2mr_o^2}{\hbar^2}x}} \frac{dx}{\sqrt{4Ex^2 - (x^2 \pm \hbar\omega_o)^2}}, \quad (21)$$

and $x_{2,1}^{(-)} = \sqrt{E} \pm \sqrt{E - \hbar\omega_{E_o}}$, $x_{2,1}^{(+)} = \pm\sqrt{E} + \sqrt{E + \hbar\omega_{E_o}}$.

The first (second) term in eqn (19) corresponds to the phonon emission (absorption). We evaluate τ^{-1} for the lower conduction band at the K-point of the BZ for MoS_2, $MoSe_2$, $MoTe_2$, WS_2, WSe_2 and WTe_2 materials. The scattering rate values given by eqn (19) are governed by the effective mass, screening parameter, and phonon frequency. For comparison, the results for each material are displayed in units of W_o of the ML, in Fig. 9.

Because the phonon frequencies for the ML and 2ML are very similar for each family, comparing the results for those compounds with the same anion is possible. In all cases, τ^{-1} is smaller in the bilayer structures. The sequence of values from lowest to highest in the SR seen in Fig. 9 is related to the increase of the r_o parameter when passing from the S to Te anion (see Table 3). Fig. 9 for the ML resembles the values obtained in ref. 51.

V. Conclusions

We have performed first principles calculations to examine the phonon dispersion curves for single-layer and bilayers of the MX_2 family (M = Mo, W and X = S, Se, Te). The method enables

us to examine the parameters describing the phonon dispersion and to elucidate their role on the optical branches. Based on the *ab initio* results of Fig. 1–3, we report the phonon parameters for the long-wavelength polar vibrations in bilayer TMDs for in-plane and out-of-plane motions. The latter was done by fitting the analytical phonon dispersion laws provided by the macroscopic equations obtained in the framework of the phenomenological continuum limit to the phonon dispersion obtained by first principles calculations. These results allow us to validate the analytical equations reported in Section III as a function of the phonon wave vector for all-optical phonon branches; this is one of the main achievements of this work, graphically represented in Fig. 5–8 together with the set of parameters that describe the twelve dispersion laws (see Table 1). The most significant differences between the single-layer and bilayer results are linked to the polar branches with E-symmetry. Although the phonon parameters for the other modes (polar and non-polar) are very similar, this does not happen with the curvatures of the longitudinal and transverse modes and the increase in the observed slope value Ξ when going from a ML to 2ML (compare Tables 1 and 2). All this is a consequence of the neighborhood influence on the dielectric properties of the 2D TMD. Using first principles analysis, we have derived the Pekar–Fröhlich Hamiltonian in double-layer structures in the small-phonon momentum limit. The analysis provides the strength of the PF interaction for ML (see ref. 52) and 2ML of MoS_2, $MoSe_2$, $MoTe_2$, WS_2, WSe_2 and WTe_2 semiconductors.

We have examined the intrinsic transport properties by evaluating the dispersion rate at low carrier density and high temperature. 2ML structures have a longer lifetime than ML ones. We demonstrate that the number of layers is paramount in evaluating the dispersion rate and transport properties. The quantitative picture of the scattering rate displayed in eqn (19) allows us to delineate the critical factors involved in conductivity and mobility. One particularly interesting point is to consider TMD materials in the presence of an external magnetic field where the transport of carriers is spin polarized.[59]

The reported analytical models become necessary to understand better transport properties, infrared and Raman spectroscopy. Among other topics, the generalization of the present results to the evaluation of optical phonons in 2D Moiré heterobilayers offers an attractive field to study the peculiarities of the symmetries of the optical branches, the dispersion laws, how the electron–phonon interaction is modified and the impact that these effects produce on the Raman selection rules, dielectric, optical properties and transport phenomena of these exotic structures.

Appendix A: parameters of *ab initio* calculations

In the DFPT calculations, the dynamical matrices were computed for a Γ-centered $n \times n$ q-point grid in the reciprocal lattice unit cell corresponding to the supercell that contains the ML and 2ML structures. The electron wavefunctions are

Table 3 Employed parameters for the evaluation of the out-of-plane and in-plane optical phonon dispersion relations of a bilayer of MX_2 (M = Mo, W; X = S, Se, Te). The corresponding values for a monolayer are also listed. a – Optimized lattice constant, c – interlayer distance, d – thickness of the monolayer or bilayer, r_0 – screening parameter, ε – dielectric constant and m – the electron effective constant

	MoS_2	$MoSe_2$	$MoTe_2$	WS_2	WSe_2	WTe_2
Single-layer						
a (Å)	3.1635	3.2991	3.5274	3.1627	3.2949	3.5230
c (Å)	15.9300	16.4957	17.6370	15.8137	16.4744	17.6481
r_0 (Å)	46.0353	53.4115	68.6629	41.9088	48.8415	64.87084
d (Å)	5.4816	5.9689	6.6794	5.5108	6.0037	6.6959
ε	16.8161	17.9151	20.5759	15.2315	16.2908	19.3933
Bilayer						
a (Å)	3.1647	3.3001	3.5305	3.1831	3.2964	3.5319
c (Å)	28.4820	29.2058	31.1933	28.3299	29.6674	31.7871
r_0 (Å)	93.1131	107.9929	139.0393	85.2742	98.4814	131.1408
d (Å)	11.0497	12.0003	13.3737	11.0062	12.0314	13.36
ε	16.8732	18.0168	20.8090	15.5173	16.3910	19.6489
m/m_o[a]	0.43	0.49	0.53	0.26	0.28	0.26

[a] Ref. 60.

Table 4 Parameters used for the *ab initio* calculations. Wavefunction (wf) and density (rho) cutoffs, k-point, and q-point grids[a]

	MoS_2	$MoSe_2$	$MoTe_2$	WS_2	WSe_2	WTe_2
wf cutoff (Ry)	65	80	80	100	80	80
rho cutoff (Ry)	650	800	800	800	800	800
k-mesh	12 × 12	12 × 12	12 × 12	12 × 12	15 × 15	12 × 12
q-mesh	6 × 6	6 × 6	6 × 6	6 × 6	6 × 6	6 × 6

[a] The PAW potential files used were Mo.pbe-spn-kjpaw_psl.1.0.0.UPF, W.pbe-spn-kjpaw_psl.1.0.0.UPF, S.pbe-n-kjpaw_psl.1.0.0.UPF, Se.pbe-n-kjpaw_psl.1.0.0.UPF, and Te.pbe-n-kjpaw_psl.1.0.0.UPF from ref. 50.

expanded in plane waves restricted by a kinetic energy cutoff. The electronic density is also expanded in plane waves restricted by a cutoff. For the electronic calculation, the reciprocal unit cell was sampled using a Γ-centered $m \times m$ k-point grid. The employed computational parameters for MoX_2 and WX_2 with X = S, Se and Te are summarized in Table 3 and 4. We observe that for a given TMD family the lattice constant and r_o increase as the mass of the chalcogen atom X increases. Furthermore, the screening parameter, or similarly, the in-plane polarizability, doubles its value when moving from the ML to the two-layer. The latter has an important impact on the evaluation of the PF Hamiltonian in eqn (17).

Appendix B: polar phonon: A_{2u}-symmetry

For the out-of-plane optical vibrations, eqn (4) is complemented by the Maxwell equation

$$\nabla \cdot (\boldsymbol{E}_z(\boldsymbol{\rho},z) + 4\pi \boldsymbol{P}_z(\boldsymbol{\rho},z)) = 0, \qquad (B1)$$

with P_z being the total macroscopic polarization due to the two sub-cell polarization contributions.

We assume the existence of a polarization field coupling the phonon amplitude with the macroscopic electric field in the plane. The mechanical displacement U_{ip} induces an electric field $E_{ind}(U_{ip})$, a general expression for the induced field can be taken as $E_{ind} = \alpha_{A_{2u}} U_{ip}$. Thus, for the vector polarization P_z we assume the linear constitutive phenomenological relation

$$P_z = [\alpha_{A_{2u}} U_{ip}(\rho) + \chi_e E_z(\rho, 0)]p(z), \tag{B2}$$

where χ_e is the out-of-plane electronic susceptibility[61] and $p(z)$ is the polarization density out-of-plane as given by $p(z) = 1/d$; $|z| < d/2$ and 0 if $|z| > d/2$, d the thickness of the bilayer. From eqn (B1) and taking $E_z = E_z(\rho, z) = -\nabla \varphi(\rho, z)$ it follows that

$$\nabla^2 \varphi(\rho, z) = 4\pi \nabla \cdot P_z \tag{B3}$$

$$\nabla \cdot P_z = \frac{dp(z)}{dz} \left[\alpha_{A_{2u}} U_{ip} \cdot e_z + \chi_e E_z \cdot e_z \right]. \tag{B4}$$

Poisson eqn (B3) points out that the electrostatic potential $\varphi(\rho, z)$ is due to the polarization charge $4\pi \nabla \cdot P_z$ of the polarization field, eqn (B2). Due to the translation symmetry in the plane, we can choose the electrostatic potential and vector amplitude as $\varphi(\rho, z) = \phi(z)e^{iq \cdot \rho}$, $U_{ip} = U_o e^{iq \cdot \rho}$, respectively. Therefore, $E_z(\rho, 0) \cdot e_z = -\nabla \varphi(\rho, z)\big|_{z=0} \cdot e_z = -\frac{d\phi(0)}{dz} e^{iq \cdot \rho}$ and eqn (B3) reduces to

$$\nabla^2 \varphi(\rho, z) = 4\pi \frac{dp(z)}{dz} \left[\alpha_{A_{2u}} U_o(\rho) - \chi_e \frac{d\phi(0)}{dz} \right] e^{iq \cdot \rho}. \tag{B5}$$

Considering the Fourier transform $\phi(z) = \frac{1}{2\pi} \int_{-\infty}^{\infty} \overline{\phi}(q_z) e^{iq_z z} dq_z$ from (B5) it follows that

$$\overline{\phi}(q_z) = -\frac{8\pi i}{d} \frac{\sin(q_z d/2)}{[q^2 + q_z^2]} \left[\alpha_{A_{2u}} U_{oip}(\rho) - \chi_e \frac{d\phi(0)}{dz} \right]. \tag{B6}$$

The z-component of the electric field $E_z(\rho, 0)$ is given by

$$E_z(\rho, 0) = -\frac{d\phi(0)}{dz} = -\int_{-\infty}^{\infty} \frac{iq_z}{2\pi} \overline{\phi}(q_z) dq_z. \tag{B7}$$

Inserting (B6) into (B7) we obtain

$$E_z(\rho, 0) = -\frac{4\pi}{d} \frac{\alpha_{A_{2u}} e^{-qd/2}}{1 + \chi_e \frac{4\pi}{d} e^{-qd/2}} U_o. \tag{B8}$$

In the long wavelength limit $e^{-qd/2} \approx 1$. Therefore,

$$E_z(\rho, 0) = -\frac{4\pi}{d} \frac{\alpha_{A_{2u}}}{1 + \frac{4\pi \chi_e}{d}} U_o. \tag{B9}$$

Employing the identity $\nabla \times \nabla \times U_{ip} - \nabla(\nabla \cdot U_{ip}) = -\nabla^2 U_{ip} = q^2 U_{ip}$ from eqn (4) we obtain

$$\rho_m \left(\omega^2 - \omega_{A_{02u}}^2 \right) U_o = \left(\frac{4\pi}{d} \frac{\alpha_{A_{2u}}^2}{1 + \frac{4\pi \chi_e}{d}} \pm q^2 \rho_m \beta_{A_{2u}}^2 \right) U_o, \tag{B10}$$

and the $\omega(q)$ for the A_{2u} mode is equal to

$$\omega^2 = \omega_{A_{02u}}^2 + \frac{4\pi}{d\rho_m} \frac{\alpha_{A_{2u}}^2}{1 + \frac{4\pi \chi_e}{d}} \pm q^2 \beta_{A_{2u}}^2. \tag{B11}$$

The second term on the right side of the above equation renormalizes the intrinsic oscillatory frequency ω_{A02u}

$$\omega_{A_{02u}}^2 + \frac{4\pi}{d\rho_m} \frac{\alpha_{A_{2u}}^2}{1 + \frac{4\pi \chi_e}{d}} \rightarrow \omega_{A_{2u}}^2, \tag{B12}$$

thus, the final dispersion relation eqn (5) for the A_{2u} mode is obtained.

Appendix C: polar phonon: E_u-symmetry

The total macroscopic electric field $E(\rho, z)$ in the plane satisfies the Maxwell equation

$$\nabla \cdot (E(\rho, z) + 4\pi P(\rho, z)) = 0, \tag{C1}$$

and for the macroscopic polarization $P(\rho, z)$ we have

$$P = [\alpha U_{ip}(\rho) + \alpha_2 E(\rho, 0)]p(z), \tag{C2}$$

with α_2 the polarizability in the plane. Taking $E(\rho, z) = -\nabla \varphi(\rho, z)$ and looking for the solutions as $U_{ip} = U_{oip} e^{iq \cdot \rho}$ and $E(\rho, z = 0) = E(q)e^{iq \cdot \rho}$, from eqn (13) and (C1) we have

$$\rho_m \left(\omega^2 - \omega_{E_{2u}}^2 \right) U_{oip} = -\alpha E(q) U_{oip} \pm \rho_m \beta_{E_{gl}}^2 q(q \cdot U_{oip})$$
$$\pm \rho_m \beta_{E_{gt}}^2 \left(-q(q \cdot U_{oip}) + q^2 U_{oip} \right), \tag{C3}$$

and

$$\nabla^2 \varphi + 4\pi \alpha_2 \nabla_\rho^2 \varphi(\rho, 0)p(z) = 4\pi \alpha \nabla \cdot [U_{ip}(\rho)p(z)]. \tag{C4}$$

In (C4), $\rho_{pol} = 4\pi \alpha \nabla \cdot [U_{ip}(\rho)p(z)]$ is considered as the polarization charge generated by the induced electric field $E_{ind} = \alpha U_{ip}(\rho)$. In Poisson's eqn (C4), the total charge density $\rho_T = \rho_{pol} + \rho_{ind}$ with

$$\rho_{ind} = -4\pi \alpha_2 \nabla_\rho^2 \varphi(\rho, 0)p(z), \tag{C5}$$

ρ_{ind} is the induced charge density related to polarization due to the in-plane electric field $E_\perp = -\nabla_\rho \varphi(\rho, 0)$ in the bilayer. The presence of an environment leads to a point charge at the origin that creates a field that shields the electrostatic potential $\varphi(\rho, z)$. For the solution of Poisson's eqn (C4), coupled to the mechanical equation of motion eqn (13), we take the Fourier transform

$$\varphi(\boldsymbol{\rho}, z) = \frac{1}{(2\pi)^3} \int \overline{\varphi}(\boldsymbol{q}, q_z) e^{i(\boldsymbol{q}\cdot\boldsymbol{\rho} + q_z z)} \mathrm{d}^2 q \, \mathrm{d} q_z. \quad \text{(C6)}$$

Thus, from (C4) it follows that for the Fourier transform of the electrostatic potential $\overline{\varphi}(\boldsymbol{q}) = \int_{-\infty}^{\infty} \overline{\varphi}(\boldsymbol{q}, q_z) \mathrm{d} q_z / 2\pi$ is

$$\overline{\varphi}(\boldsymbol{q}) = -\frac{2\pi}{q} \frac{\alpha F(\boldsymbol{q})}{1 + 2\pi\alpha_2 q}, \quad \text{(C7)}$$

where the long-wave length limit $qd/2 \ll 1$ was considered and

$$F(\boldsymbol{q}) = \int \nabla \cdot \left[\boldsymbol{U}_{\mathrm{ip}}(\boldsymbol{\rho}) \right] e^{-i\boldsymbol{q}\cdot\boldsymbol{\rho}} \mathrm{d}^2 \rho. \quad \text{(C8)}$$

From (C7) and (C8) the Fourier transform of $\boldsymbol{E}_{\rho}(\boldsymbol{\rho}, z = 0) = -\nabla\varphi(\boldsymbol{\rho})$ is given by

$$\boldsymbol{E}(\boldsymbol{q}) = -2\pi\alpha \frac{\boldsymbol{q}}{q} \frac{\boldsymbol{q} \cdot \boldsymbol{U}_{\mathrm{ip}}}{(1 + 2\pi\alpha_2 q)}. \quad \text{(C9)}$$

Considering $\boldsymbol{U}_{\mathrm{oip}} = \boldsymbol{U}_{\mathrm{l}} + \boldsymbol{U}_{\mathrm{t}}$ as the longitudinal and transverse independent components of the vector displacement we obtain the $\omega(q)$ laws dictated by eqn (14) and (15).

Appendix D: Pekar–Fröhlich Hamiltonian

Here we discuss the formulation of PF coupling valid for a bilayer of TMD. The lattice vibration, U_{ip} gives rise to the 2D macroscopic electric field $\boldsymbol{E}_{\perp} = -\nabla_{\rho}\varphi(\boldsymbol{\rho}, 0)$. An electric charge $-e$ is coupled to the scalar potential $\varphi(\boldsymbol{\rho})$, so the PF Hamiltonian can be written as

$$\hat{H}_{\mathrm{PF}} = -e\hat{\varphi}(\boldsymbol{\rho}). \quad \text{(D1)}$$

The polarization charge $\rho_{\mathrm{T}} = \rho_{\mathrm{pol}} + \rho_{\mathrm{ind}}$ is responsible for the scalar potential φ as discussed in Appendix C. From eqn (C6) and (C7) immediately follows

$$\varphi(\boldsymbol{\rho}) = -\frac{\alpha}{2\pi} \int \frac{F(\boldsymbol{q})}{q(1 + 2\pi\alpha_2 q)} e^{i\boldsymbol{q}\cdot\boldsymbol{\rho}} \mathrm{d}^2 q. \quad \text{(D2)}$$

Transforming the classical field of the phonon amplitude $\boldsymbol{U}_{\mathrm{ip}}$ into a quantum-field operator $\hat{\boldsymbol{U}}_{\mathrm{ip}}(\boldsymbol{\rho})$ in terms of phonon creation ($\hat{\boldsymbol{b}}_q^{\dagger}$) and annihilation ($\hat{\boldsymbol{b}}_q$) phonon operator we obtain

$$\hat{\boldsymbol{U}}_{\mathrm{ip}} = \sum_q \frac{\boldsymbol{q}}{q} \left(\frac{\hbar}{2\rho_{\mathrm{m}} S \omega_{\mathrm{gl}}} \right)^{1/2} \left[\hat{b}_q e^{i\boldsymbol{q}\cdot\boldsymbol{\rho}} + \hat{b}_q^{\dagger} e^{-i\boldsymbol{q}\cdot\boldsymbol{\rho}} \right], \quad \text{(D3)}$$

with $S = N_{\mathrm{c}} A$ the normalization area, A the area of the sub-unit cell and N_{c} the number of cells. Consequently, $F(\boldsymbol{q}) \to \hat{F}(\boldsymbol{q})$ and $\varphi(\boldsymbol{\rho}) \to \hat{\varphi}(\boldsymbol{\rho})$.

Inserting eqn (D3) into eqn (C8), the in-plane electrostatic potential, eqn (D2), is given by

$$\hat{\varphi} = i \sum_q \left(\frac{2\pi^2 \hbar \alpha^2}{S \rho_{\mathrm{m}} \omega_{\mathrm{gl}}} \right)^{1/2} \frac{1}{(1 + 2\pi\alpha_2 q)} \left[\hat{b}_q e^{i\boldsymbol{q}\cdot\boldsymbol{\rho}} + \hat{b}_q^{\dagger} e^{-i\boldsymbol{q}\cdot\boldsymbol{\rho}} \right]. \quad \text{(D4)}$$

From eqn (D1) and (D4) follows the Hamiltonian, eqn (17).

Conflicts of interest

There are no conflicts to declare.

Acknowledgements

References

1 S. Manzeli, D. Ovchinnikov, D. Pasquier, O. V. Yazyev and A. Kis, *Nat. Rev. Mater.*, 2017, **2**, 17033.

2 B. Schönfeld, J. J. Huang and S. C. Moss, *Acta Crystallogr., Sect. B: Struct. Sci.*, 1983, **39**, 404–407.

3 S. Coutinho, M. Tavares, C. Barboza, N. Frazão, E. Moreira and D. L. Azevedo, *J. Phys. Chem. Solids*, 2017, **111**, 25–33.

4 Z. Huang, W. Zhang and W. Zhang, *Materials*, 2016, **9**, 716.

5 J. K. Ellis, M. J. Lucero and G. E. Scuseria, *Appl. Phys. Lett.*, 2011, **99**, 261908.

6 Y. Zhang, T.-R. Chang, B. Zhou, Y.-T. Cui, H. Yan, Z. Liu, F. Schmitt, J. Lee, R. Moore, Y. Chen, H. Lin, H.-T. Jeng, S.-K. Mo, Z. Hussain, A. Bansil and Z.-X. Shen, *Nat. Nanotechnol.*, 2014, **9**, 111–115.

7 Z. G. Yu, B. I. Yakobson and Y.-W. Zhang, *ACS Appl. Energy Mater.*, 2018, **1**, 4115–4121.

8 C. D. English, G. Shine, V. E. Dorgan, K. C. Saraswat and E. Pop, *Nano Lett.*, 2016, **16**, 3824–3830.

9 W. Wu, D. De, S.-C. Chang, Y. Wang, H. Peng, J. Bao and S.-S. Pei, *Appl. Phys. Lett.*, 2013, **102**, 142106.

10 H.-L. Liu, C.-C. Shen, S.-H. Su, C.-L. Hsu, M.-Y. Li and L.-J. Li, *Appl. Phys. Lett.*, 2014, **105**, 201905.

11 E. Singh, P. Singh, K. S. Kim, G. Y. Yeom and H. S. Nalwa, *ACS Appl. Mater. Interfaces*, 2019, **11**, 11061–11105.

12 S. Rashidi, S. Rashidi, R. K. Heydari, S. Esmaeili, N. Tran, D. Thangi and W. Wei, *Progr. Photovolt.: Res. Appl.*, 2021, **29**, 238–261.

13 C. Wang, F. Yang and Y. Gao, *Nanoscale Adv.*, 2020, **2**, 4323–4340.

14 A. Taffelli, S. Dirè, A. Quaranta and L. Pancheri, *Sensors*, 2021, **21**, 2758.

15 W. Zheng, X. Liu, J. Xie, G. Lu and J. Zhang, *Coord. Chem. Rev.*, 2021, **447**, 214151.

16 Y. Hu, Y. Huang, C. Tan, X. Zhang, Q. Lu, M. Sindoro, X. Huang, W. Huang, L. Wang and H. Zhang, *Mater. Chem. Front.*, 2017, **1**, 24–36.

17 E. C. Ahn, *npj 2D Mater. Appl.*, 2020, **4**, 17.

18 Y. Liu, N. O. Weiss, X. Duan, H.-C. Cheng, Y. Huang and X. Duan, *Nat. Rev. Mater.*, 2016, **1**, 16042.

19 A. H. Castro Neto, F. Guinea, N. M. R. Peres, K. S. Novoselov and A. K. Geim, *Rev. Mod. Phys.*, 2009, **81**, 109–162.

20 E. Suárez Morell, J. D. Correa, P. Vargas, M. Pacheco and Z. Barticevic, *Phys.Rev. B: Condens. Matter Mater. Phys.*, 2010, **82**, 121407.

21 Y. Cao, V. Fatemi, S. Fang, K. Watanabe, T. Taniguchi, E. Kaxiras and P. Jarillo-Herrero, *Nature*, 2018, **556**, 43–50.

22 K. Yasuda, X. Wang, K. Watanabe, T. Taniguchi and P. Jarillo-Herrero, *Science*, 2021, **372**, 1458–1462.

23 D. Zhang, P. Schoenherr, P. Sharma and J. Seidel, *Nat. Rev. Mater.*, 2022, **8**, 25–40.

24 Y. Wang, S. Jiang, J. Xiao, X. Cai, D. Zhang, P. Wang, G. Ma, Y. Han, J. Huang, K. Watanabe, T. Taniguchi, Y. Guo, L. Wang, A. S. Mayorov and G. Yu, *Front. Phys.*, 2022, **17**, 43504.

25 E. A. Cortés, J. M. Florez and E. S. Morell, *J. Phys. Chem. Solids*, 2023, **173**, 111086.

26 X. Wang, K. Yasuda, Y. Zhang, S. Liu, K. Watanabe, T. Taniguchi, J. Hone, L. Fu and P. Jarillo-Herrero, *Nat. Nanotechnol.*, 2022, **17**, 367–371.

27 B. Huang, G. Clark, D. R. Klein, D. MacNeill, E. Navarro-Moratalla, K. L. Seyler, N. Wilson, M. A. McGuire, D. H. Cobden, D. Xiao, W. Yao, P. Jarillo-Herrero and X. Xu, *Nat. Nanotechnol.*, 2018, **13**, 544–548.

28 E. S. Morell, A. León, R. H. Miwa and P. Vargas, *2D Mater.*, 2019, **6**, 025020.

29 H. Li, Z. Yin, Q. He, H. Li, X. Huang, G. Lu, D. W. H. Fam, A. I. Y. Tok, Q. Zhang and H. Zhang, *Small*, 2012, **8**, 63–67.

30 S. Das, H.-Y. Chen, A. V. Penumatcha and J. Appenzeller, *Nano Lett.*, 2013, **13**, 100–105.

31 S. Kim, A. Konar, W.-S. Hwang, J. H. Lee, J. Lee, J. Yang, C. Jung, H. Kim, J.-B. Yoo, J.-Y. Choi, Y. W. Jin, S. Y. Lee, D. Jena, W. Choi and K. Kim, *Nat. Commun.*, 2012, **3**, 1011.

32 H. Terrones and M. Terrones, *J. Mater. Res.*, 2014, **29**, 373–382.

33 X. Liu, D. Qu, J. Ryu, F. Ahmed, Z. Yang, D. Lee and W. J. Yoo, *Adv. Mater.*, 2016, **28**, 2345–2351.

34 K. M. McCreary, M. Phillips, H.-J. Chuang, D. Wickramaratne, M. Rosenberger, C. S. Hellberg and B. T. Jonker, *Nanoscale*, 2022, **14**, 147–156.

35 G. Fiori, F. Bonaccorso, G. Iannaccone, T. Palacios, D. Neumaier, A. Seabaugh, S. K. Banerjee and L. Colombo, *Nat. Nanotechnol.*, 2014, **9**, 768–779.

36 Q. H. Wang, K. Kalantar-Zadeh, A. Kis, J. N. Coleman and M. S. Strano, *Nat. Nanotechnol.*, 2012, **7**, 699–712.

37 C. Chakraborty, L. Kinnischtzke, K. M. Goodfellow, R. Beams and A. N. Vamivakas, *Nat. Nanotechnol.*, 2015, **10**, 507–511.

38 B. Radisavljevic, A. Radenovic, J. Brivio, V. Giacometti and A. Kis, *Nat. Nanotechnol.*, 2011, **6**, 147–150.

39 E. H. Hwang and S. Das Sarma, *Phys. Rev. B: Condens. Matter Mater. Phys.*, 2008, **77**, 235437.

40 A. Kefayati, J. P. Bird and V. Perebeinos, *Phys. Rev. B*, 2022, **106**, 155415.

41 C. Trallero-Giner, D. G. Santiago-Pérez and V. M. Fomin, *Sci. Rep.*, 2023, **13**, 292.

42 N. A. Pike, A. Dewandre, B. Van Troeye, X. Gonze and M. J. Verstraete, *Phys. Rev. Mater.*, 2019, **3**, 074009.

43 I. Paradisanos, G. Wang, E. M. Alexeev, A. R. Cadore, X. Marie, A. C. Ferrari, M. M. Glazov and B. Urbaszek, *Nat. Commun.*, 2021, **12**, 538.

44 X. Li, J. T. Mullen, Z. Jin, K. M. Borysenko, M. Buongiorno Nardelli and K. W. Kim, *Phys. Rev. B: Condens. Matter Mater. Phys.*, 2013, **87**, 115418.

45 J. K. Han, M.-A. Kang, C.-Y. Park, M. Lee, S. Myung, W. Song, S. S. Lee, J. Lim and K.-S. An, *Nanotechnology*, 2019, **30**, 335402.

46 S. Baroni, S. de Gironcoli, A. Dal Corso and P. Giannozzi, *Rev. Mod. Phys.*, 2001, **73**, 515–562.

47 P. Giannozzi, S. Baroni, N. Bonini, M. Calandra, R. Car, C. Cavazzoni, D. Ceresoli, G. L. Chiarotti, M. Cococcioni, I. Dabo, A. dal Corso, S. de Gironcoli, S. Fabris, G. Fratesi, R. Gebauer, U. Gerstmann, C. Gougoussis, A. Kokalj, M. Lazzeri, L. Martin-Samos, N. Marzari, F. Mauri, R. Mazzarello, S. Paolini, A. Pasquarello, L. Paulatto, C. Sbraccia, S. Scandolo, G. Sclauzero, A. P. Seitsonen, A. Smogunov, P. Umari and R. M. Wentzcovitch, *J. Phys.: Condens. Matter*, 2009, **21**, 395502.

48 J. Klimeš, D. R. Bowler and A. Michaelides, *Phys. Rev. B: Condens. Matter Mater. Phys.*, 2011, **83**, 195131.

49 T. Thonhauser, S. Zuluaga, C. A. Arter, K. Berland, E. Schröder and P. Hyldgaard, *Phys. Rev. Lett.*, 2015, **115**, 136402.

50 A. Dal Corso, *Comput. Mater. Sci.*, 2014, **95**, 337–350.

51 T. Sohier, M. Calandra and F. Mauri, *Phys. Rev. B*, 2017, **96**, 75448.

52 N. Scheuschner, R. Gillen, M. Staiger and J. Maultzsch, *Phys. Rev. B: Condens. Matter Mater. Phys.*, 2015, **91**, 235409.

53 C. Trallero-Giner, E. Menéndez-Proupin, E. S. Morell, R. Pérez-Álvarez and D. G. Santiago-Pérez, *Phys. Rev. B*, 2021, **103**, 235424.

54 X. Zhang, X.-F. Qiao, W. Shi, J.-B. Wu, D.-S. Jiang and P.-H. Tan, *Chem. Soc. Rev.*, 2015, **44**, 2757–2785.

55 A. V. Kolobov and J. Tominaga, *Two-Dimensional Transition-Metal Dichalcogenides*, Springer International Publishing Switzerland, 2016, vol. 239.

56 M. Yamamoto, S. T. Wang, M. Ni, Y.-F. Lin, S.-L. Li, S. Aikawa, W.-B. Jian, K. Ueno, K. Wakabayashi and K. Tsukagoshi, *ACS Nano*, 2014, **8**, 3895–3903.

57 P. Y. Yu and M. Cardona, *Fundamentals of Semiconductors*, Springer, Berlin Heidelberg, 2010.

58 K. Kaasbjerg, K. S. Thygesen and K. W. Jacobsen, *Phys. Rev. B: Condens. Matter Mater. Phys.*, 2012, **85**, 115317.

59 J. R. Schaibley, H. Yu, G. Clark, P. Rivera, J. S. Ross, K. L. Seyler, W. Yao and X. Xu, *Nat. Rev. Mater.*, 2016, **1**, 16055.

60 A. Kormányos, G. Burkard, M. Gmitra, J. Fabian, V. Zólyomi, N. D. Drummond and V. Fal'ko, *2D Mater.*, 2015, **2**, 022001.

61 J.-Z. Zhang, *AIP Adv.*, 2020, **10**, 045316.